# Inviscid Hypersonic Flow Around Blunt Bodies

ELLIOTT D. KATZEN* AND GEORGE E. KAATTARI†
*NASA Ames Research Center, Moffett Field, Calif.*

**Approximate methods have been used to study the inviscid flow in the subsonic region of the shock layer about blunt bodies. Effects of high angles of attack, nonequilibrium flow, and vapor injection were investigated. The results for equilibrium flow indicated that, as the flight speed was increased for a body at high angles of attack, the shock wave distorted as well as translated toward the body. These changes were accompanied by a movement of the stagnation point toward the corner of the body and an increase in the pressure gradients. Thus, it was noted that significant errors in convective and radiative heating distributions result if the assumption is made that wind-tunnel tests using cold air or helium adequately represent flight conditions at atmosphere-entry speeds. The effect of nonequilibrium flow on shock-layer thickness was calculated for a manned, lifting entry body; for flight conditions when heating was severe, the effect was small. The results for flows with various gases injected into the shock layer indicated large increases in shock-standoff distances as a result of the injection. Such increases must be taken into account in analyzing the heating for meteoric bodies or vehicles entering the Earth's atmosphere at meteoric speeds.**

## Nomenclature

$d$ = maximum diameter of body, m
$g$ = acceleration, m/sec$^2$
$h$ = altitude, km
$K$ = reaction rate constant, sec$^{-1}$
$M$ = Mach number
$m$ = molecular weight of mixture, g/mole
$m_0$ = molecular weight of undissociated and un-ionized gas, g/mole
$R$ = radius of shock or body, m
$r$ = radial coordinate of shock or body, m
$s$ = arc length, m
$T$ = temperature, °K
$V$ = speed, m/sec
$x$ = coordinate of shock measured from plane normal to body axis at location $\Delta_0$, m
$Z$ = molecular weight ratio, $m_0/m$
$\alpha$ = angle of attack, deg
$\Delta$ = shock standoff, m
$\delta$ = dummy variable
$\theta_i$ = inclination of interface at point opposite sonic point on body
$\rho$ = density, kg/m$^3$
$\bar{\rho}$ = average density, kg/m$^3$
$\varphi$ = angular coordinate (see Fig. 2), deg

### *Subscripts*

$b$ = body
$bs$ = basic shock
$e$ = equilibrium
$f$ = frozen
$g$ = injected gas
$i$ = interface
$m$ = maximum value
$ne$ = nonequilibrium
0 = body axis value at $\alpha = 0$, value with no vapor injection, and value at sea level
st = stagnation point
$\infty$ = freestream condition
2 = immediately behind shock, where the shock is normal to the freestream direction
* = value at sonic point

Presented at the AIAA Entry Technology Conference, Williamsburg and Hampton, Va., October 12–14, 1964 (no preprint number; published in bound volume of preprints of the meeting); revision received April 1, 1965.

* Assistant Chief, Gasdynamics Branch. Associate Fellow Member AIAA.
† Research Scientist.

## Introduction

THE inviscid flow in the subsonic region of the shock layer about a blunt body at hypersonic speeds has received considerable attention, but solutions have been available only for very limited cases. Solutions for equilibrium flow have been available for certain restricted classes of bodies at zero angle of attack (e.g., Refs. 1 and 2, which span an interval of six years of work in this field) and, for a very limited number of cases, for angles of attack. In Ref. 3, small angles of attack are treated; an approximate method for high angles of attack is presented in Ref. 4. However, only limited results are presented in Ref. 4. For spherical bodies, limited solutions have also been available for nonequilibrium flow[5, 6] and for flow with vapor injection.[7, 8] For arbitrary shapes, however, methods have not been available for predicting the effects of nonequilibrium flow, high angles of attack, or vapor injection.

The purpose of the paper is threefold: 1) to outline briefly approximate methods that allow prediction of the effects of high angle of attack, nonequilibrium flow chemistry, and vapor injection on the subsonic flow field of a blunt body in the hypersonic speed range; 2) to present results in terms of shock-wave shape and location, stagnation-point location, and surface pressure for equilibrium flow, and in terms of shock-wave shape and location for nonequilibrium flow, and flow with vapor injection; and 3) to compare, where possible, these results with available experiment or more exact theory.

## Methods

For equilibrium flow, the method of Ref. 4 is used for predicting the shock-layer thickness at angles of attack and the

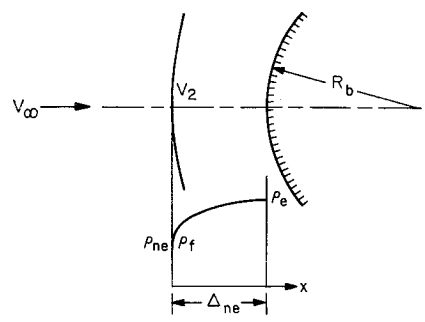


**Fig. 1 Nonequilibrium flow.**

location of the stagnation point, Ref. 9 is used for the surface-pressure distributions, and Ref. 10 is used for predicting the shock-layer thickness at zero angle of attack. Extensions of Ref. 10 are used for predicting the effects of nonequilibrium flow and vapor injection. The methods are based on 1) the application of continuity of mass flow between the shock wave and the body surface, 2) relationships for oblique and normal shock waves, and 3) a correlation of stagnation-point velocity gradient with normal-shock density ratio for various axisymmetric bodies, similar to the correlation of Ref. 11 of stagnation-point velocity gradient with Mach number and ratio of specific heats. For convenience, the methods are referred to hereafter as the approximate method.

### Nonequilibrium Flow

The basis of the method for nonequilibrium flow is the assumption that the shock standoff in the stagnation region is a function of a mean nonequilibrium density evaluated along the stagnation streamline from the shock wave to the body. This assumption is made because for equilibrium flow the shock standoff at the stagnation point correlates on the basis of normal-shock density ratio for a wide variety of bodies. The energy processes considered in the method are vibration, dissociation, and ionization.

To define the mean nonequilibrium density, the local density, velocity, and flow time must be related. The local nonequilibrium density is assumed to increase exponentially with time or distance (see Fig. 1):

$$\rho_{ne} = \rho_e - (\rho_e - \rho_f)e^{-Kt} \tag{1}$$

This is approximately the type of density variation calculated in Ref. 12. The rate constant $K$ is a function of the flight speed and altitude. In the present instance, $K$ is determined from an unpublished correlation made by D. R. Chapman, of the NASA Ames Research Center, of the rate data of Refs. 13–16. An approximate expression for the rate constant is $K = 1.29 \times 10^{-14}\,(\rho_\infty/\rho_0)V_\infty{}^6$. The nonequilibrium results of Ref. 12 indicate an approximately linear variation of velocity in the region between the shock and the stagnation point. Therefore, the velocity is assumed to vary as

$$V = V_2[1 - (x/\Delta_{ne})] \tag{2}$$

where $\Delta_{ne}$ is the shock standoff at the stagnation point. The flow time is

$$t = \int_0^\delta \frac{dx}{V_2[1 - (x/\Delta_{ne})]} \tag{3}$$

Now that expressions are available for the local density, velocity, and flow time, the mean nonequilibrium density can be obtained. When Eqs. (2) and (3) are substituted in Eq. (1), the local nonequilibrium density becomes

$$\rho_{ne} = \rho_e - (\rho_e - \rho_f)[1 - (\delta/\Delta)]^{K\Delta_{ne}/V_2} \tag{4}$$

The mean density is

$$\begin{aligned}\bar{\rho}_{ne} &= \frac{1}{\Delta_{ne}}\int_0^{\Delta_{ne}} \rho_{ne}\,d\delta \\ &= \frac{1}{\Delta_{ne}}\int_0^{\Delta_{ne}} \left\{\rho_e - (\rho_e - \rho_f)\left[1 - \frac{\delta}{\Delta_{ne}}\right]^{K\Delta_{ne}/V_2}\right\} d\delta \\ &= \rho_e - \left[\frac{V_2}{K\Delta_{ne} + V_2}\right](\rho_e - \rho_f)\end{aligned} \tag{5}$$

Equation (5) contains the unknown $\Delta_{ne}$ on the right, and an iteration procedure must be used to solve for $\bar{\rho}_{ne}$.

For hemispheres, the mean nonequilibrium density can be obtained in a more convenient form by making the further approximation $\Delta \propto \rho_\infty/\rho$. This has been found to be a reasonable assumption for hemispheres. With the use of the foregoing approximation, $\Delta_{ne} = (\rho_f/\rho_{ne})\Delta_f$, where $\Delta_f$ is the shock standoff corresponding to frozen flow. Substituting for $\Delta_{ne}$ in Eq. (5) gives

$$\frac{\bar{\rho}_{ne}}{\rho_f} = \frac{\left\{\left[\frac{\Delta_f K}{V_2} - 1\right]^2 + 4\,\frac{\rho_e}{\rho_f}\left(\frac{\Delta_f K}{V_2}\right)\right\}^{1/2} - \left[\frac{\Delta_f K}{V_2} - 1\right]}{2} \tag{6}$$

The mean shock-density ratio is $\bar{\rho}_{ne}/\rho_\infty = (\rho_f/\rho_\infty)(\bar{\rho}_{ne}/\rho_f)$, and $V_2 = \rho_\infty V_\infty/\rho_f$. When these quantities are substituted in Eq. (6),

$$\frac{\bar{\rho}_{ne}}{\rho_\infty} = \left(\frac{\rho_f}{\rho_\infty}\right) \times \frac{\left\{\left[\left(\frac{\Delta_f K}{V_\infty}\right)\frac{\rho_f}{\rho_\infty} - 1\right]^2 + 4\,\frac{\rho_e}{\rho_\infty}\left(\frac{\Delta_f K}{V_\infty}\right)\right\}^{1/2} - \left[\left(\frac{\Delta_f K}{V_\infty}\right)\frac{\rho_f}{\rho_\infty} - 1\right]}{2} \tag{7}$$

Now that the mean shock density is in hand, the shock standoff is determined as for equilibrium flow.

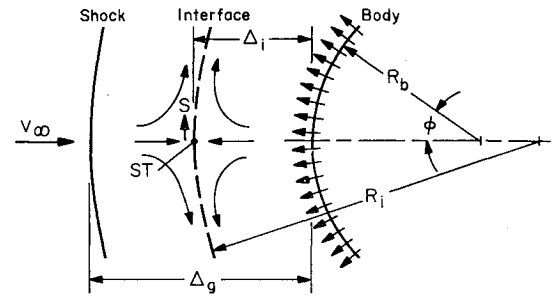


**Fig. 2 Flow with vapor injection.**

### Flow with Vapor Injection

In order to provide a tractable analysis of the complicated flows that arise when vapors are injected into the shock layer, certain approximations and assumptions must be made. The assumptions made in the present analysis are similar to those of Ref. 7, but the analyses are different. The postulated model of the flow is shown in Fig. 2. The body through which the gas is injected has a spherical face of radius $R_b$. It is assumed that an interface exists which separates the gas (air) passing through the shock and the vapors injected into the shock layer; the interface is assumed to be spherical, of radius $R_i$. It is also assumed that heat conduction between the two flows is negligible and that the pressures of the air and the injected gas are identical at the interface. The velocity of the injected vapor $V_g$ is arbitrarily taken to vary with $\varphi$ as $V_{g\varphi} = V_{g\varphi=0}\cos\varphi$. This should be a good approximation for the variation of velocity of ablating gas with angular position for convective heating. However, the radiative heating rate falls off much faster with distance from the stagnation point than does the convective heating rate.[17] Thus, for radiative heating the variation of velocity would be quite different from that assumed. It is further assumed that the gas is injected at subsonic speed and that the flow in the vapor layer is incompressible.

With the aid of the foregoing approximations and assumptions, the two flows can be related along the interface. Since the pressures are equal along the interface, the equations of state for the two flows yield

$$\rho_g = (m_{0g}/m_0)(Z/Z_g)(T/T_g)\rho \tag{8}$$

where the quantities without the subscript $g$ are located on

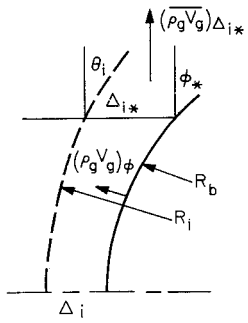


**Fig. 3 Control area.**

the left side of the interface (Fig. 2); the Bernoulli equation for incompressible flow reduces to

$$\rho V^2 = \rho_g V_g^2 \tag{9}$$

Combining Eqs. (8) and (9) yields

$$\rho_g V_g = [(m_{0g}/m_0)(Z/Z_g)(T/T_g)]^{1/2}\rho V \tag{10}$$

Thus, at the stagnation point the relationship between the gradients of mass flow for the two flows is

$$\frac{d(\rho_g V_g/\rho_* V_*)}{d(s/s_*)} = \left[\left(\frac{m_{0g}}{m_0}\right)\left(\frac{Z}{Z_g}\right)\left(\frac{T}{T_g}\right)\right]^{1/2}\frac{d(\rho V/\rho_* V_*)}{d(s/s_*)} \tag{11}$$

where equations for $d(\rho V/\rho_* V_*)/d(s/s_*)$ and $\rho_* V_*$ are given in Ref. 10.

With the two flows related along the interface, continuity of mass flow for the vapor layer is satisfied in a manner analogous to that in Ref. 10. First, a relationship is written for continuity of mass flow for a small cylindrical element of volume, of radius $dy$, and length extending from the body to the interface

$$\pi(dy)^2(\rho_g V_g)_{\varphi=0} = 2\pi dy\,\Delta_i\,\frac{[d(\rho_g V_g)_i + d(\rho_g V_g)_b]_{\varphi=0}}{2} \tag{12}$$

Equation (11) provides the gradient of mass flow at the interface; a linear variation of mass flow is assumed between the interface and the body. The result is

$$\frac{\Delta_i}{R_b} = \frac{1}{1 + \dfrac{[(m_{0g}/m_0)\ (Z/Z_g)\ (T/T_g)^{1/2}\sin\theta_i\ d(\rho V/\rho_* V_*)}{\theta_i \sin\varphi_*}\ \dfrac{(\rho_* V_*/\rho_\infty V_\infty)}{d(s/s_*)\ \ (\rho_g V_g/\rho_\infty V_\infty)}} \tag{13}$$

The angle $\theta_i$ corresponds to the angle of inclination of the sonic point for a sphere and is given in Ref. 9.

An additional continuity relationship is written in order to determine the inclination of the point on the body opposite the sonic point on the interface $\varphi_*$ and the interface standoff $\Delta_i$. The control area (Fig. 3) is cylindrical, of radius $y = R_b \sin\varphi_*$ and length $\Delta_{i*}$. The mass flow into the element is given by

$$2\pi R_b^2 \int_0^{\varphi_*} (\rho_g V_g)_{\varphi=0} \sin\varphi\cos\varphi\, d\varphi = \pi R_b^2 (\rho_g V_g)_{\varphi=0}\sin^2\varphi_* \tag{14}$$

The arithmetic mean flow normal through $\Delta_{i*}$ is

$$\langle\rho_g V_g\rangle_{\Delta i*} = \tfrac{1}{2}\{[(m_{0g}/m_0)(Z/Z_g)(T/T_g)]^{1/2}\rho_* V_* \cos\theta_i + (\rho_g V_g)_{\varphi=0}\cos\varphi_* \sin\varphi_*\} \tag{15}$$

Combining Eqs. (14) and (15) gives

$$R_b/\Delta_{i*}(1 - \cos\varphi_*)\sin\varphi_* = [(m_{0g}/m_0)(Z/Z_g)(T/T_g)]^{1/2} \times \{[(\rho_* V_*)/(\rho_\infty V_\infty)]/[(\rho_g V_g)/(\rho_\infty V_\infty)]\}\cos\theta_i \tag{16}$$

An additional unknown, $\Delta_{i*}$, has been introduced. However, a geometric relationship exists between $\Delta_i$ and $\Delta_{i*}$:

$$\Delta_{i*}/R_b = (\Delta_i/R_b) + (1 - \cos\varphi_*) - \sin\varphi_* \tan(\theta_i/2) \tag{17}$$

Sufficient equations are now available to define the shape and location of the interface and the shock. Equations (13, 16, and 17) can be used to determine the unknowns $\varphi_*$ and $\Delta_i/R_b$ as functions of $[(\rho_g V_g)/(\rho_\infty V_\infty)][(m_0/m_{0g})(Z_g/Z)(T_g/T)]^{1/2}$. The orientation of the interface can be determined from $R_i = (R_b \sin\varphi_*)/(\sin\theta_i)$. The shock-wave shape and location are calculated for an equivalent solid hemisphere of radius $R_i$.

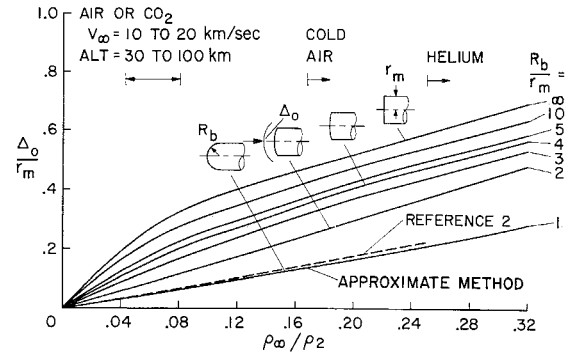


**a) Shock standoff**

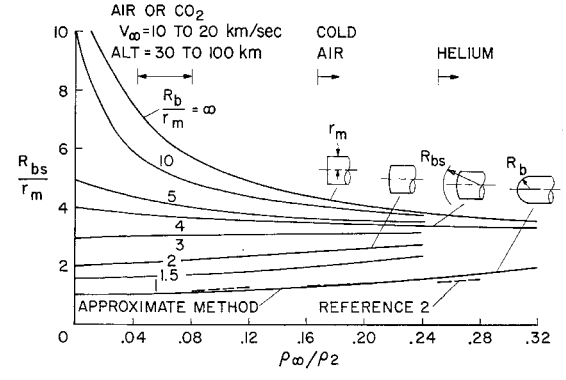


**b) Shock radius**

**Fig. 4 Shock shape for zero angle of attack, equilibrium flow.**

Now that a solution for hemispheres is in hand, it is further assumed that the results of the effect of vapor injection for hemispheres can be applied, in ratio form, to hemispherical segments.

## Results and Discussion

### Equilibrium Flow

Results for equilibrium flow are presented for bodies having sharp corners and front surfaces which vary from a hemisphere $R_b/r_m = 1$ to a flat face $R_b/r_m = \infty$.

#### *Shock-layer thickness*

Figure 4 was prepared to facilitate the construction of shock-layer thickness for zero angle of attack. The shock standoff (Fig. 4a) and the shock radius (Fig. 4b) are required to define the shock shape at zero angle of attack. They are presented as functions of the normal-shock density ratio $\rho_\infty/\rho_2$, which depends upon the flight speed, the flight altitude, and the atmospheric constituents.

A wide range of flight conditions is represented by the range of normal-shock density ratios shown in Fig. 4. Normal-shock density ratios for high-speed entries into the atmospheres of Earth and Mars are indicated to orient the reader to the relationship between flight conditions and density ratio. Limiting density ratios for wind-tunnel tests in helium or cold air are also indicated.

Shock-layer thicknesses for hemispheres calculated by the approximate method and by the more exact numerical

method of Ref. 2 are compared in Fig. 4. The results of Ref. 2 (the dashed lines) are for ideal gases and real air. The ideal-gas conditions are for a range of ratios of specific heat $\gamma$ from 1.1 to 1.67 and Mach numbers from 5 to 100. The real-air flows correspond to speeds from 3 to 14 km/sec and altitudes from 30 to 90 km. Reference 2 has shown that the shock standoff for hemispheres correlates on the basis of normal-shock density ratio for a wide range of conditions. Figure 4 indicates that the shock radius correlates on the same basis but not as well as does shock standoff. The agreement between the results of the approximate method and the exact method is satisfactory.

The relatively linear dependence of shock standoff on density ratio for hemispheres shown in Fig. 4a has been observed by others. In fact, this linearity has been used as a basis for extrapolating shock shapes from wind-tunnel tests using cold air or helium to high-speed flight conditions. Note, however, that, for the blunter bodies, the shock standoff does not have a linear dependence on density ratio.

The approximate method is used in Fig. 5 to show the effect of angle of attack on the shock-layer thickness for a flat-face body. Shock-wave shapes in the vertical plane of symmetry are presented. The density ratio is 0.25, which corresponds to the flow of cold air at a Mach number of about 3. As the angle of attack is increased from 0° to 30°, the shock rotates about the body axis and approaches attachment at the windward corner. Note that at angle of attack the shock-wave shape is distorted from the shape at zero angle of attack is not easily characterized by a standoff distance and a radius, as is the case at zero angle of attack.

A comparison of a predicted and measured shock-wave shape for $\alpha = 30°$ is also shown in Fig. 5. The experimental data are from the Ames 1- × 3-ft supersonic wind tunnel. Note that, for $\alpha = 30°$, the predicted shock-wave shape is beginning to have an inflection point at the lower part. This is a region in which the predicted and experimental curves are beginning to diverge. It is noted in Ref. 4 that this occurrence of an inflection point is one of the conditions that limits the angle of attack for which the method is applicable. It can be seen that the predicted and experimental shocks agree reasonably well at the stated limit of applicability.

In Fig. 6a, the approximate method shows the influence of flight speed on the shock-wave shape for a flat-faced body at $\alpha = 20°$. The shock-wave shape for a speed of approximately 1 km/sec ($\rho_\infty/\rho_2 = 0.25$) is repeated from Fig. 5, and shock-wave shapes for speeds up to approximately 20 km/sec are added for comparison. As the flight speed is increased, the shock wave translates toward the body; the curvature of the shock wave is decreased a small but significant amount.

A comparison is shown in Fig. 6b of shock waves computed by the approximate method and by a commonly used procedure for extrapolating shock waves from data for low speeds to entry flight speeds. In the procedure often used, the shock wave is scaled according to the relationship $\Delta \propto \rho_\infty/\rho_2$. A shock wave scaled in this manner is shown by the dashed curve. The simple scaling procedure does not agree with the present method. Reconsideration of Fig. 4a indicates that this is to be expected for this type body. The reader will recall that, for a body with a flat face, the shock standoff cannot be expressed as a linear function of density.

Instead of scaling the shock standoff by a linear relationship as in the foregoing, it would seem reasonable to consider scaling the shock standoff for $\alpha \neq 0°$ according to the relationships for $\alpha = 0°$ shown in Fig. 4a. This scaling procedure forces the calculated and the scaled shock-wave shapes to agree at the longitudinal axis of symmetry of the body. It can be seen from Fig. 6b that this scaling procedure (the dash-dot curve) is an improvement over the procedure of scaling according to the linear relationship. However, the scaled shock wave is rotated less toward the body than the shock wave predicted by the approximate method.

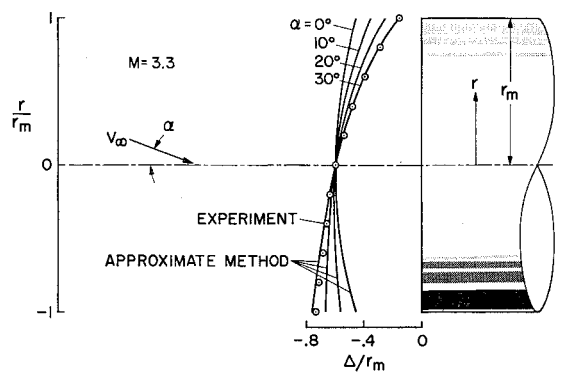


**Fig. 5 Effect of angle of attack on the shock-layer thickness, equilibrium flow; $\rho_\infty/\rho_2 = 0.25$.**

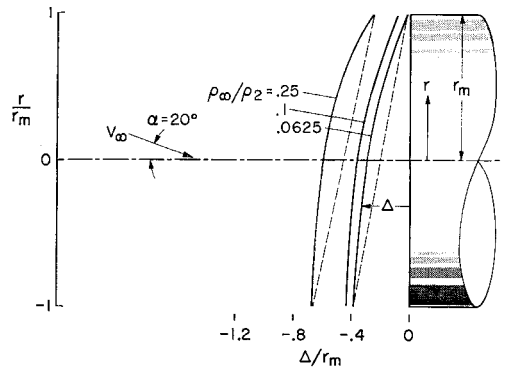


**a) Approximate method; $R_b/r_m = \infty$**

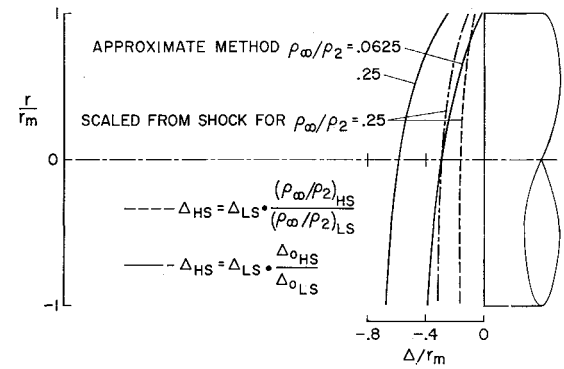


**b) Comparison of scaling procedure and approximate method; $R_b/r_m = \infty$**

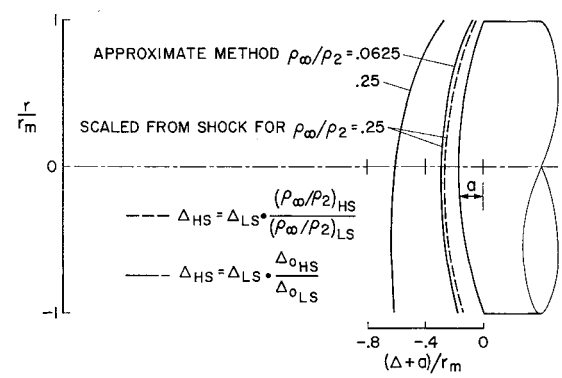


**c) Comparison of scaling procedure and approximate method; $R_b/r_m = 3$**

**Fig. 6 Effect of density ratio on shock-layer thickness equilibrium flow; $\alpha = 20°$.**

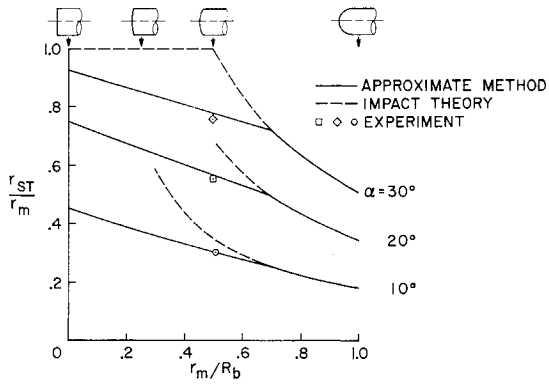


a) Body curvature; $\rho_\infty/\rho_2 = 0.25$

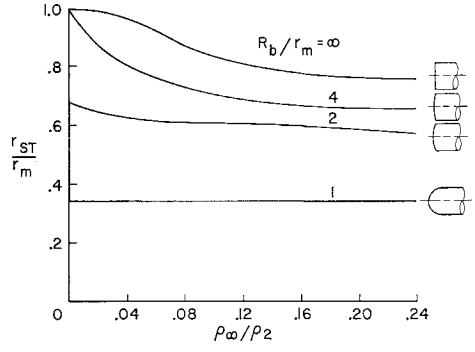


b) Density ratio; $\alpha = 20°$

**Fig. 7 Effect of body curvature and density ratio on stagnation-point location, equilibrium flow.**

Figure 6c presents a comparison of scaled and predicted shock waves for a body less blunt than that considered in Fig. 6b ($R_b/r_m = 3$ instead of $R_b/r_m = \infty$). The differences in the computed shock-wave shape and the shock-wave shape scaled in proportion to the density ratio are less than those for the body with a flat face, but the differences are significant. The predicted shock-wave shape and the shock-wave shape scaled in proportion to the ratio $(\Delta_{0\text{ high speed}})/(\Delta_{0\text{low speed}})$ are in excellent agreement. Thus, the usefulness of the simple scaling procedure varies with the bluntness of the body.

### *Location of stagnation point*

The influence of the radius of curvature of the body on the location of the stagnation point is shown in Fig. 7a. Results are presented for angles of attack of 10°, 20°, and 30°; the density ratio is 0.25. For a given angle of attack, the stagnation point moves toward the corner as the bluntness is increased.

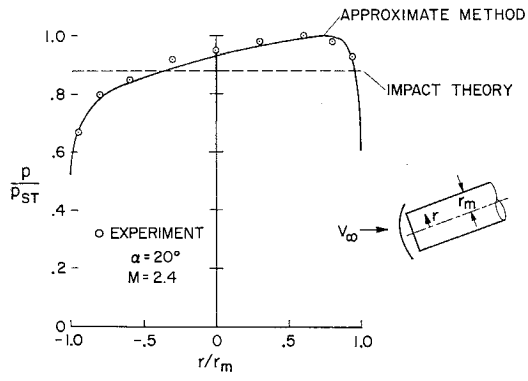


**Fig. 8 Comparison of predicted and measured body pressures, equilibrium flow.**

Figure 7a also compares stagnation-point locations predicted by the approximate method with those predicted by impact theory and, for a particular body, those determined from experiments. For front surfaces that are complete or nearly complete hemispheres, $\frac{2}{3} \lesssim r_m/R_b < 1$, the approximate method and impact theory are in agreement; the stagnation point is normal to the freestream velocity. For the bodies that are more blunt than the hemisphere, however, the impact theory fails to anticipate the effect of the corner, and the stagnation point predicted by this method is too close to the corner. The results of the approximate method are in good agreement with experimental results for the body with $R_b/r_m = 2$. The experimental results were obtained in the NASA Ames 1- × 3-ft supersonic wind tunnel.

The influence of flight speed (through density ratio) on the location of the stagnation point is shown in Fig. 7b. The results presented are for an angle of attack of 20°. For this angle of attack and a body whose front surface is a hemisphere, the stagnation point is constant with changes in density ratio or flight speed. This is not true for bodies that are more blunt than the hemisphere. Thus, it should be noted that a significant error in the location of the stagnation point and, therefore, in heating distribution results if the assumption is made that the experimental values obtained from typical wind-tunnel tests with helium or cold air ($0.17 < \rho_\infty/\rho_2 < 0.25$) adequately represent results that would be attained in flight at atmospheric-entry speeds ($\rho_\infty/\rho_2 \approx 0.06$).

### *Pressure distribution*

Figure 8 provides a comparison of predicted and measured pressures (unpublished wind-tunnel measurements by Seiff and Stalder). It shows an example of a case for which rigorous equilibrium solutions have not been available and for which the widely used impact theory does not provide correct answers. The example is for the pressure distribution on the face of a flat-face cylinder at $\alpha = 20°$. It can be seen that in contrast with impact theory, which predicts a uniform pressure on the flat face, the approximate method predicts the correct distribution of pressure.

It is of interest to observe the effects of flight speed on the surface-pressure distribution of a body that is more blunt than a hemisphere. It is well known that the pressure distribution for a hemisphere changes very little with changes in flight speed. Figure 9 again shows the pressure distribution for a body with a flat face at an angle of attack of 20°; the density ratios are 0.25 (corresponding to tests in helium or cold air) and 0.06 (corresponding to atmosphere-entry flight speeds). The effect of changes in flight speed is largest near the windward corner. The pressures in this region change much more rapidly with distance for the high-speed flight condition than for low speeds. The attendant increase in velocity gradients must be taken into account in assessing the effects of flight speed on the heating to the body.

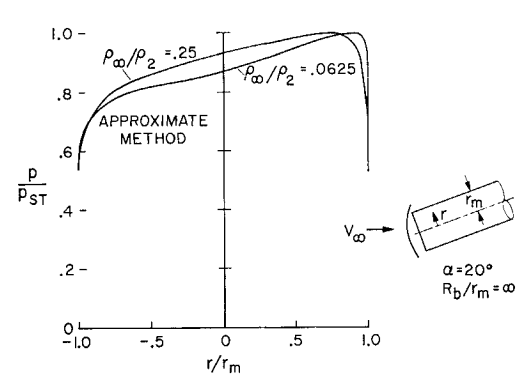


**Fig. 9 Effect of density ratio on the pressure distribution, equilibrium flow; $\alpha = 20°$, $R_b/r_m = \infty$.**

### Nonequilibrium Flow

The shock-wave standoff distance for a spherical body obtained by the present approximate method has been compared with the results of other methods and with experimental results. Comparisons with the machine-computed solutions of Hall, Eschenroeder, and Marrone[5] are shown in Fig. 10; good agreement is noted. Other comparisons made but not shown indicate that the present results are also in agreement with the predictions of Freeman[12] and with the experimental results of Lobb.[18]

Figure 10 also shows the predicted influence of flight speed and altitude and of hemisphere diameter on the nonequilibrium effects on shock-wave standoff. At the higher flight speeds, the shock-wave standoff distance approaches the equilibrium value, even though the time of flow from the shock to the body is decreased with increased flight speed. This phenomenon has been explained by Shih et al.[19] on the basis that the higher temperatures in the shock layer, at the higher speeds, accelerate the chemical reactions.

The nonequilibrium flow for a typical lifting entry body on an undershoot trajectory is now considered. The shock standoff is presented in Fig. 11 for a body of about 3-m diam, which is sufficiently large to contain men. The angle of attack of the body is 30°, and the entry speed is equal to Earth escape speed. The lift-drag ratio of the vehicle is 0.5. Lifting vehicles on undershoot trajectories that are deceleration-limited generally plunge into the atmosphere and skip out of the atmosphere unless they are prevented from doing so. For the case shown, the body is allowed to skip to an altitude of 150 km after peak heating and peak deceleration (10 $g$). The body then plunges back to lower depths. The time periods that are important for heating are indicated in the figure. For these time periods and the conditions shown, the shock standoffs are not greatly different from the corresponding equilibrium values.

Shock-standoff distances are shown in Fig. 12 for the same body as just mentioned on an overshoot trajectory for which the body is at constant altitude of 80 km for a large part of the time. (The maximum deceleration for this trajectory is 2 $g$.) Heating is important during most of this overshoot trajectory. It can be seen that again the shock standoffs are not greatly different from the corresponding values for equilibrium flow.

The heating to an atmosphere-entry body is related to the radiation intensity and the volume of the shock layer. For the body and trajectories just studied, calculations of total heating based on the gas-cap volumes for equilibrium flow should not be grossly in error.

### Flow with Vapor Injection

Experiments were conducted to study flows with various gases injected into the shock layer of a blunt body. The purpose of the experiments was to provide a basis for assessing

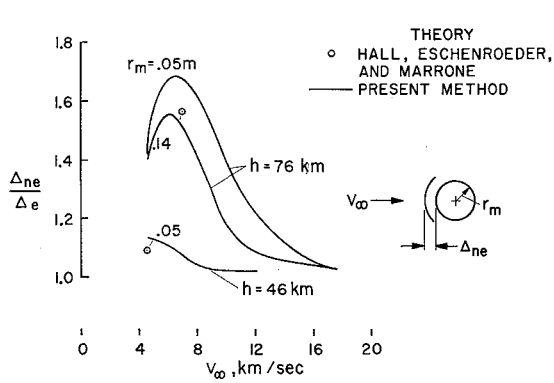


Fig. 10 Shock standoff for hemispheres, nonequilibrium flow.

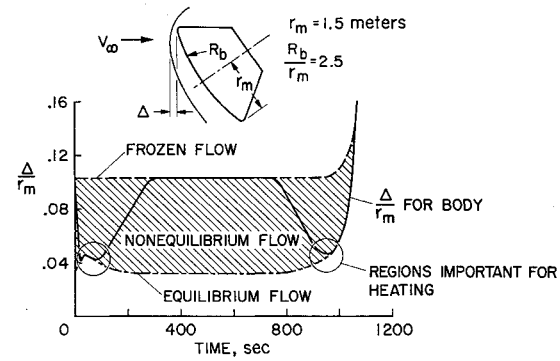


Fig. 11 Shock standoff for typical lifting body; undershoot trajectory with skip to altitude of 150 km.

the assumptions and the results of the method of prediction. In particular, it was desired to see whether an interface exists between the injectant and the test stream. The tests were conducted in the NASA Ames 1- × 3-ft supersonic wind tunnel. The test stream was air, for which the freestream Mach number was 5. The gases injected into the shock layer were freon, helium, and air. The injectant and air temperatures were approximately the same and were not sufficiently high for the gases to be dissociated or ionized. The body had a porous, spherical face with $R_b/r_m = 2$.

Photographs in Fig. 13 illustrate different types of flow patterns that depend principally upon the gas injected and whether the gas is injected into the shock layer at subsonic or supersonic speeds. Figure 13a gives an example of a flow in which freon was injected into the shock layer at subsonic speeds. There is a distinct but irregular interface between the injected gas and the oncoming air; the interface is approximately spherical. The same type of flow pattern is illustrated in Fig. 13b. In this example, the helium injection speed was subsonic. An instance in which helium was injected at supersonic speed is illustrated in Fig. 13c; the forward shock is conical. One wonders whether the effect of this type of flow pattern for a body in high-speed flight would be to reduce the radiative heating to the body.[20] If this were the case, it might be possible to design a passive heat-protection system (i.e., an ablation system) for a blunt vehicle which would be suitable for entry speeds for which convective and radiative heating rates are generally prohibitive. An example is shown in Fig. 13d of air injection at supersonic speed. A secondary shock wave can be seen between the body and the upstream shock wave. For either subsonic or supersonic air injection, it is difficult to detect an interface from the photographs.

Figure 14 illustrates the large effect on shock-standoff distance of the injection of various gases into the shock layer. Shock-standoff distances are shown with freon, helium, and air injected into the shock layer at either subsonic or supersonic speeds. When the vapors leave the body at super-

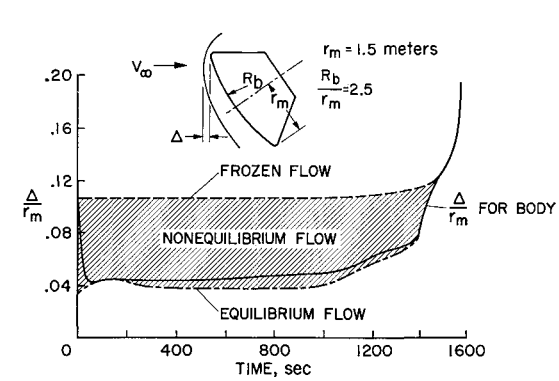


Fig. 12 Shock standoff for typical lifting body; overshoot trajectory with altitude limited to 80 km.

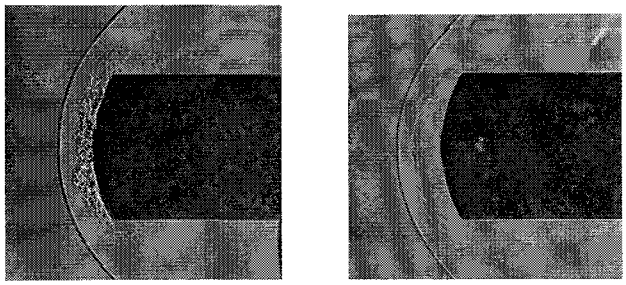

a) Freon; $M_g < 1$ b) Helium; $M_g < 1$

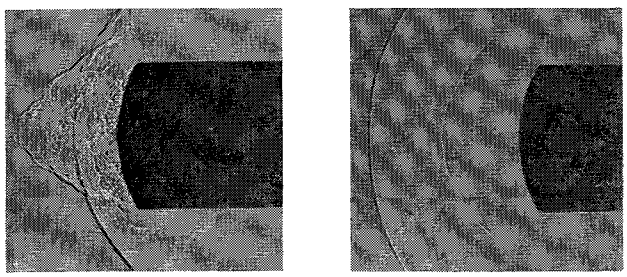

c) Helium; $M_g < 1$ d) Air; $M_g > 1$

**Fig. 13 Flows with various gases injected into the shock layer; $M_\infty = 5$(air).**

sonic speeds but at flow rates the same as for subsonic speeds, the standoff distance is greater than for subsonic speeds.

A comparison is also shown in Fig. 14 of the predicted and measured effect on shock standoff for the subsonic injection of gases into the shock layer. The results are shown as a function of

$$(\rho_g V_g/\rho_\infty V_\infty)\,[(\rho_2/\rho_\infty)(m_0/m_{0g})(Z_g/Z)(T_g/T)]^{1/2}$$

which correlates the present calculated results for various gases and flight conditions. An approximate expression for this correlation is

$$\Delta_g/\Delta_0 \cong 1 + (\rho_g V_g/\rho_\infty V_\infty)\,[(\rho_2/\rho_\infty) \times (m_0/m_{0g})(Z_g/Z)(T_g/T)]^{1/2} \quad (18)$$

A correlation of the theoretical results of Cresci and Libby[7] is also shown in Fig. 14. This correlation was obtained by multiplying the parameter $N_3$ (used in Ref. 7) by $\rho_2/\rho_\infty$. The results of both methods agree well with the experimental results.

Calculations have been made of the shock-standoff distance for a meteoric body entering the Earth's atmosphere at a speed of 20 km/sec. The ablative products were assumed to be silicon dioxide. The calculations indicate that the injection is at subsonic speeds; the standoff distance is increased by a factor of about 2 over the nonablating case. Such increases must be taken into account in analyzing the total heating for meteoric bodies or for vehicles entering the Earth's atmosphere at meteoric speeds.

## Concluding Remarks

Approximate methods have been used to predict the inviscid flow in the subsonic region of the shock layer about blunt bodies. Results have been presented for the equilibrium and nonequilibrium flow of real gases about various body shapes at high angles of attack. Also, a limited treatment of the effect of vapor injection into the shock layer has been given.

For equilibrium flow, the parameters studied were shock-wave shape and location, stagnation-point location, and surface-pressure distribution. The bodies had sharp corners and front surfaces that varied from a hemisphere to a flat face. It was found that, as the flight speed was increased, for

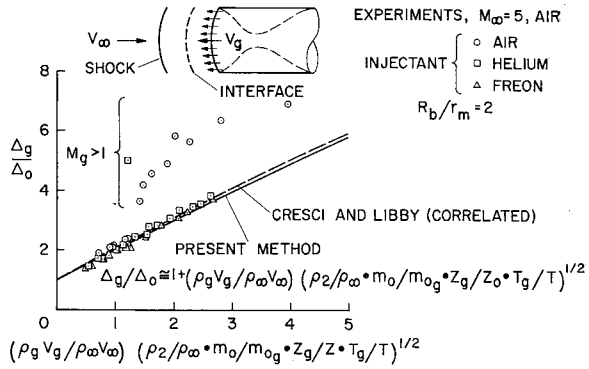


**Fig. 14 Effect of vapor injection on shock standoff.**

the more blunt bodies at high angles of attack, the shock wave distorted, as well as translated, toward the body. These changes were accompanied by a movement of the stagnation point toward the corner of the body and an increase in the pressure gradients. Thus, it was noted that significant errors in convective and radiative heating distributions result if the assumption is made that wind-tunnel tests using cold air or helium adequately represent flight conditions at atmosphere-entry speeds.

Shock standoffs at the stagnation point were calculated for the equilibrium and nonequilibrium flow about a body entering the Earth's atmosphere at a speed equal to Earth escape speed. The lift-drag ratio of the body was 0.5; maximum decelerations were between 2 and 10 $g$, and the body was sufficiently large for manned missions. During the periods of the trajectories when the heating was severe, the shock standoffs for nonequilibrium flow were not greatly different from the corresponding values for equilibrium flow.

Shock standoffs at the stagnation point were also studied for flows with various gases injected into the shock layers of nonlifting bodies whose front surfaces consisted of spherical segments. Large increases in shock-standoff distance were indicated as a result of the injection. Such increases must be taken into account in analyzing the total heating for meteoric bodies or vehicles entering the Earth's atmosphere at meteoric speeds.

## References

[1] Gravalos, F. G., Edelfelt, I. H., and Emmons, H. W., "The supersonic flow about a blunt body of revolution for gases at chemical equilibrium," General Electric Co. Missle and Space Vehicle Div. GE-MSVD TISR58SD245 (June 1958).

[2] Lomax, H. and Inouye, M., "Numerical analysis of flow properties about blunt bodies moving at supersonic speeds in an equilibrium gas," NASA TR R-204 (1964).

[3] Swigart, R. J., "Hypersonic blunt-body flow fields at angle of attack," AIAA J. **2**, 115–117 (1964).

[4] Kaattari, G. E., "Shock envelopes of blunt bodies at large angles of attack," NASA TN D-1980 (1963).

[5] Hall, J. G., Eschenroeder, A. Q., and Marrone, P. V., "Blunt-nose inviscid airflows with coupled nonequilibrium processes," J. Aerospace Sci. **29**, 1038–1051 (1962).

[6] Ellington, D., "Approximate method for hypersonic nonequilibrium blunt body airflows," AIAA J. **1**, 1901–1904 (1963).

[7] Cresci, R. J. and Libby, P. A., "The downstream influence of mass transfer at the nose of a slender cone," J. Aerospace Sci. **29**, 815–826 (1962).

[8] Howe, J. T. and Sheaffer, Y. S., "Mass addition in the stagnation region for velocity up to 50,000 feet per second," NASA TR R-207 (1964).

[9] Kaattari, G. E., "Predicted gas properties in the shock layer ahead of capsule-type vehicles at angles of attack," NASA TN D-1423 (1962).

[10] Kaattari, G. E., "Predicted shock envelopes about two types of vehicles at large angles of attack," NASA TN D-860 (1961).

[11] Traugott, S. C., "An approximate solution of the direct supersonic blunt-body problem for arbitrary axisymmetric shapes," J. Aerospace Sci. **27**, 361–370 (1960).

[12] Freeman, N. C., "Non-equilibrium flow of an ideal dissociating gas," J. Fluid Mech. 4, 407–425 (1958).
[13] Wray, K. L., "Chemical kinetics of high temperature air," Avco Research Rept. 104 (June 1961).
[14] Lin, S. C., Fyfe, W. I., and Neal, R. A., "Rate of ionization behind shock waves in air," Avco Research Rept. 105 (September 1960).
[15] Allen, R. A., Keck, J. C., and Camm, J. C., "Non-equilibrium radiation from shock heated nitrogen and a determination of the recombination rate," Avco Research Rept. 110 (June 1961).
[16] Teare, J. D., Georgiev, S., and Allen, R. A., "Radiation from the non-equilibrium shock front," Avco Research Rept. 112 (October 1961).
[17] Wick, B. H., "Radiative heating of vehicles entering the earth's atmosphere," *The High Temperature Aspects of Hypersonic Flow*, edited by W. C. Nelson (Pergamon Press, New York, 1963), pp. 607–627.
[18] Lobb, R. K., "Experimental measurement of shock detachment distance on spheres fired in air at hypervelocities," Ref. 17, pp. 519–527.
[19] Shih, W. C. L. and Baron, J. R., "Nonequilibrium blunt-body flow using the method of integral relations," AIAA J. 2, 1062–1071 (1964).
[20] Allen, H. J., Seiff, A., and Winovich, W., "Aerodynamic heating of conical entry vehicles at speeds in excess of earth parabolic speed," NASA TR R-185 (1963).

JULY 1965 AIAA JOURNAL VOL. 3, NO. 7

# Studies of Wakes of Support-Free Spheres at $M = 16$ in Helium

IRWIN E. VAS,* EARLL M. MURMAN,† AND SEYMOUR M. BOGDONOFF‡
*Princeton University, Princeton, N. J.*

**A detailed investigation of the flow field behind spheres magnetically suspended in a Mach 16 helium stream has been initiated. Pitot pressure and constant-current hot-wire measurements have been employed to investigate a region from 1 to 50 body diameters downstream of two sphere diameters, 0.75 and 0.375 in., and several body Reynolds numbers from 45,400 to 109,000. Previous data reported in the literature indicated that transition to turbulence should occur within the region of investigation, but hot-wire voltage measurements lead to the conclusion that the wake is probably laminar. Detailed radial and axial pitot pressure distributions are presented and compared with two-dimensional cylinder data at the same Mach number, ballistic-range data, and two theories. The measured rms hot-wire fluctuation voltage was constant at a very low value along the wake axis but showed peaks at the wake edge.**

## Nomenclature

| | | |
|---|---|---|
| $D$ | = | body diameter |
| $D_w$ | = | wake diameter |
| $f$ | = | frequency |
| $M$ | = | Mach number |
| $p$ | = | static pressure |
| $P_t$ | = | pitot pressure |
| $P_0$ | = | stagnation-chamber pressure |
| $Re = \rho u/\mu$ | = | Reynolds number per unit length |
| $T_{aw}$ | = | adiabatic recovery temperature |
| $T_0$ | = | stagnation-chamber temperature |
| $T_w$ | = | hot-wire temperature |
| $u$ | = | velocity |
| $V_{\text{rms}}$ | = | root-mean-square hot-wire fluctuation voltage |
| $X$ | = | radial distance measured from wake axis |
| $Y$ | = | radial distance measured from wake axis |
| $Z$ | = | axial distance measured from sphere center |
| $\rho$ | = | density |
| $\mu$ | = | molecular viscosity coefficient |
| $\tau$ | = | hot-wire time constant |

*Subscripts*

| | | |
|---|---|---|
| $\text{℄}$ | = | evaluated at wake centerline |
| $e$ | = | evaluated at wake edge |
| $\infty$ | = | evaluated in freestream |
| $(\ )_*$ | = | conditions when flow traversing normal shock at $M_\infty$ has expanded back to $p_\infty$ |

Presented at the AIAA 2nd Aerospace Sciences Meeting, New York, N. Y., January 25–27, 1965. This study was sponsored by the Advanced Research Projects Agency (Ballistic Missile Defense Office) and technically administered by the Fluid Dynamics Branch of the Office of Naval Research under Contract No. Nonr-1858(37). The program was also partially supported by the Aerospace Research Laboratories, Office of Aerospace Research, U. S. Air Force, Wright-Patterson Air Force Base, Ohio, under Contract No. AF 33(615)-1079.

* Research Engineer, Gas Dynamic Laboratory. Member AIAA.
† NASA Fellow, Gas Dynamics Laboratory. Associate Member AIAA.
‡ Professor, Head of Gas Dynamics Laboratory. Fellow Member AIAA.

## 1. Introduction

DURING the past several years, the interest in the area of hypersonic wakes has resulted in a large number of both theoretical and experimental investigations of the wake flow region. The key motivation for these studies is the desire to predict the flow properties in the wakes of vehicles reentering the earth's atmosphere as a method of analyzing the long observable trails.

Hypersonic flow fields are generally divided into two classes comprising blunt and slender bodies. The limiting case of an axisymmetric blunt-body flow field is well represented by that of a spherical body (Fig. 1). Curvature of the bow-shock wave results in a highly rotational flow-field downstream of it. The fluid in the viscous boundary layer, which has traversed a strong, nearly normal shock wave, separates from the body and forms a free shear layer. After passing through a compression region known as the "neck," the separated boundary layer forms a hot viscous trail or wake. If the wake is laminar, it grows via molecular diffusion into a region of varying entropy. If the wake is turbulent, growth is accomplished through turbulent diffusion. The hot wake is cooled through two mechanisms: expansion and conduction. The expansion from a relatively high-pressure area around the neck region to freestream ambient pressure causes the temperature of the wake to decrease. This effect is aug-